applied sciences

MDPI

Article

Nonlinear Simulation of Terminal Maneuvers Including Landing Gear Dynamics, Crosswind and Ground Effect

Stefano Cacciola * and Andrea Calabria

Department of Aerospace Science and Technology, Politecnico di Milano, Via La Masa 34, 20156 Milan, Italy; andreacalabria.1809@gmail.com

* Correspondence: stefano.cacciola@polimi.it

Abstract

Terminal flight phases, particularly landing, are among the most critical, due to low altitude, low speed and the possible presence of crosswinds. Tools capable of accurately modeling and simulating these phases are essential for identifying potential issues and assessing airplane safety integrity. This work focuses on the development of a nonlinear flight simulator devised to handle terminal maneuvers, including ground effect and wind. Such a simulator incorporates the six-degree-of-freedom rigid body equations of motion coupled with a landing gear model and with a basic control that emulates the action of the pilot, while the aircraft aerodynamic characteristics are estimated through a dedicated semi-empirical procedure. The proposed simulator is employed to assess the effect of crosswind and approach speed on different performance indicators, considering a general aviation airplane (Ryan Navion). These indicators include ground roll distance, wing-tip clearance and lateral forces exerted on the landing gear. The results demonstrate that landings are achievable even beyond the demonstrated crosswind limits without encountering wing-tip strikes or rollover and that higher approach speeds could be advisable in strong crosswind conditions.

Keywords: flight dynamics; terminal maneuvers; simulation; crosswind; landing gear; ground effect

1. Introduction

Landing is one of the most critical phases of a flight because the aircraft operates at low altitude and speed, while external disturbances, most notably wind, may bring the airplane into dangerous conditions due to the proximity to the terrain [1,2]. The safety of landing maneuvers is ensured by effective and consolidated airport procedures, improved weather awareness, and the use of automatic controls for approach and landing; however, despite these precautions, the final phases, particularly landing, still remain critical for flight safety. As noted in the Flight Safety Foundation (FSF) report, a better knowledge of flight dynamics near the ground may improve safety during crosswind terminal maneuvers [3].

For this reason, accurate modeling of takeoff, landing, and the associated airborne phases is essential to analyze the aircraft behavior in these conditions and identify potential safety concerns.

Although simple simulation methods, based on lumped elements, are accurate enough for many applications, such as preliminary aircraft design, to provide a general understanding of aircraft behavior during takeoff and landing, a more sophisticated modeling approach is necessary when analyzing realistic terminal maneuvers. This is particularly

Academic Editors: Rosario Pecora, Jérôme Morio, Dongsheng Wen and Jin Zhao

Received: 23 December 2025
Revised: 29 January 2026
Accepted: 2 February 2026
Published: 7 February 2026

true in windy conditions, where several factors must be considered. First, the kinematics of the aircraft movement must be accurately reproduced, as touchdown or liftoff may occur asymmetrically, with one leg making contact first. Second, the contact between each leg and the ground requires consideration of the nonlinear dynamics of the landing gear and tires, including their interaction with the ground. Third, the variation in aerodynamic properties due to ground effects, affecting lift, drag, and moment coefficients, must be appropriately reproduced. Similarly, configuration changes, such as landing gear and flap extraction or retraction, must also be accounted for in the aerodynamic modeling. Finally, the influence of the ground proximity on the aerodynamic properties must be adequately captured [4].

Notable examples of tools for simulating landing maneuvers can be found in [5–8], where landing gear dynamic models of different complexities were proposed. Tire dynamics are analyzed in [9], where the authors concluded that even simple models with low computational costs may provide good approximations in the case of contact over flat surfaces. A tire friction model is introduced in [10], and subsequently used in [11,12] for landing simulations.

In order to develop a general-purpose terminal maneuver simulator, aircraft and landing gear and tire dynamics shall be integrated, finding a good compromise between modeling complexity and computational costs, as suggested in [6,13,14]. This goal is far from trivial, as in the literature, many simulators neglect the modifications of the aerodynamics induced by the ground effect [6,7,15].

The aim of this work is to develop a nonlinear flight simulator tailored to terminal maneuvers, capable of adequately handling both takeoff and landing, as well as all airborne flight conditions. This simulator is built upon the one described in Ref. [15], utilizing standard rigid-body dynamics equations to model the aircraft motion, with its orientation parameterized using Cardan angles. The rigid-body dynamics are supplemented by the dynamics of the tires and landing gear, along with a specialized function to detect which landing gear leg, if any, has contacted the ground. The simulator proposed in [15], despite its overall capabilities, used a simplified aerodynamic model that was fully linear and based on constant stability and control derivatives, even if significant variations in the aerodynamic parameters due to ground proximity are expected. Furthermore, the model omitted nose-wheel steering, which is crucial for maintaining directional control after touchdown, particularly under strong crosswind conditions. These limitations prevent an accurate simulation of a complete terminal maneuver, restricting the use of the simulator to only a few seconds before and after touchdown, i.e., during a phase where nose-wheel steering is not employed and the changes in the aerodynamics due to ground effect can be ignored.

The work presented in this paper addresses these limitations by incorporating a dedicated tool to model the aircraft aerodynamics, partially based on Digital Datcom [16]. Due to certain limitations of the Datcom software (https://www.pdas.com/datcomdownload.html, last accessed on 3 April 2025), such as analyzing only one movable surface at a time, the derivation of the aerodynamic model is performed through multiple analyses in a prescribed process, as also suggested for unusual configurations [17]. Moreover, the simulator includes a simplified pilot model, implemented through simple proportional controls. These controls manage all actions required in terminal phases, including flare, braking and steering of the nosewheel to maintain the alignment of the airplane with the runway during terminal phases.

The main findings of this work can be summarized as follows:

- Variation of the aerodynamic coefficients due to ground effect must be taken into account to adequately simulate takeoff and landing maneuvers.

- The impact of ground effect on the moment coefficient is of paramount importance, as nose-down or nose-up moments can be experienced as airplanes approach the terrain.
- To reduce lateral loads on the landing gear during landing in strong crosswind conditions, it is advisable to slightly increase the approach speed at the expense of an increased ground run and a reduced wing-tip clearance, aspects that can be easily managed to avoid safety issues.
- A comprehensive aerodynamic model of an airplane, even if based on semi-empirical methodologies, coupled with a suitable flight dynamics simulator, can help engineers explore potentially critical conditions, such as landing in strong crosswind, that were not encountered during the flight testing executed for airplane certification.

The paper is organized according to the following plan. Section 2 introduces the reference aircraft used for all computations, the Ryan Navion. The procedure to compute the aerodynamic database through the semiempirical methodologies is provided in Section 3, while Section 4 details the developed simulation environment. Several terminal maneuvers are simulated to illustrate the effects of ground proximity and evaluate terminal performance indices in Section 5, including a takeoff simulation, landing in calm air and crosswind conditions. Section 6 deals with a parametric study on landings under varying crosswind intensities and approach speeds. Finally, Section 7 summarizes the main results obtained in this work and provides insights into potential improvements and future developments.

2. Reference Aircraft

The reference aircraft for this thesis, used for all the proposed analyses, is the Ryan Navion. The Ryan (originally North American) Navion is a single-engine, retractable-gear, four-seat aircraft originally designed and built by North American Aviation in the 1940s. The airplane features a standard back-tail configuration with a low wing characterized by a significant dihedral angle. Figure 1 shows a three-view of the airplane, taken from Ref. [18]. Tables 1 and 2 report the main geometry and inertia properties of the reference airplane, while Table 3 deals with the landing gear properties, which were derived from the Navion tire specifications [19].

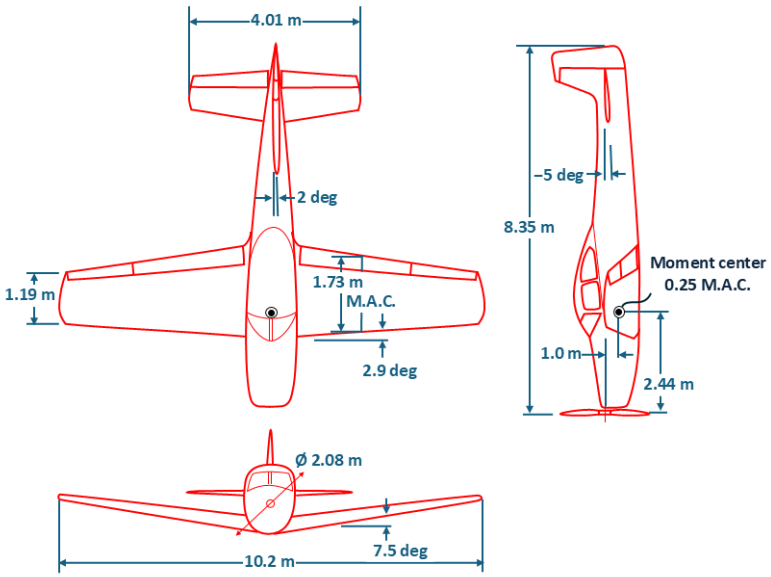

Figure 1. Ryan Navion three-view (based on [18]).

Table 1. Ryan Navion geometric parameters.

	Parameter	Symbol	Value
Wing	Wing area	S	17.112 m^2
	Mean aerodynamic chord	c	1.74 m
	Wingspan	b	10.20 m
	Aspect ratio	AR	6.04
	Taper ratio	λ	0.54
	Sweep angle, leading edge	Λ_{LE}	2.996 deg
	Dihedral angle	Γ	7.5 deg
	Tail incidence	i_w	2 deg
	Twist angle	α_{twist}	-3 deg
	Tip airfoil		NACA 6410 R
	Root airfoil		NACA 4415 R
Horizontal tail	Area	S^{HT}	4.0 m^2
	Aspect ratio	AR^{HT}	4.0
	Taper ratio	λ^{HT}	0.67
	Sweep angle, leading edge	Λ_{LE}^{HT}	6 deg
	Wing incidence	i_{HT}	-1 deg
	Airfoil		NACA 0012
Vert. tail	Area (above HT)	S^{VT}	1.163 m^2
	Tip airfoil		NACA 0012.04
	Root airfoil		NACA 0013.2

Table 2. Ryan Navion inertia properties [18].

Parameter	Symbol	Value
Mass	m	1293 kg
Center of gravity position		25% c
Moments of inertia	J_x	1742.33 kg m^2
	J_y	3762.4 kg m^2
	J_z	4389.10 kg m^2
	J_{xz}	0 kg m^2

Table 3. Ryan Navion landing gear properties.

Parameter	Symbol	Value
Main Gear attachment longitudinal position with respect to CG in body axes	$x^{\mathcal{B}}_{\mathcal{S}/\mathcal{B}_{MG}}$	-0.33 m
Main Gear attachment lateral position with respect to CG in body axes	$y^{\mathcal{B}}_{\mathcal{S}/\mathcal{B}_{MG}}$	1.33 m
Main Gear attachment vertical position with respect to CG in body axes	$z^{\mathcal{B}}_{\mathcal{S}/\mathcal{B}_{MG}}$	0.28 m
Main Gear leg assembly mass	m_{MG}	25.9 kg
Main Gear shock absorber stroke	$\delta_{s_{MG}}$	0.23 m
Main Gear shock absorber length	$L_{s_{0_{MG}}}$	0.55 m
Main Gear shock absorber cylinder diameter	$d_{c_{MG}}$	0.045 m
Main Gear shock absorber orifice diameter	$d_{o_{MG}}$	0.0025 m
Main Gear shock absorber internal volume	$V_{0_{MG}}$	1.83×10^{-4} m^3
Main Gear shock absorber preload pressure	$P_{0_{MG}}$	1.8×10^5 Pa
Orifice discharge coefficient	c_d	0.61
Main Gear tire undeformed radius	$r_{t_{0_{MG}}}$	0.255 m

Table 3. *Cont.*

Parameter	Symbol	Value
Main Gear tire equivalent stiffness coefficient	$k_{t_{MG}}$	5.64×10^5 N/m
Main Gear tire equivalent damping coefficient	$c_{t_{MG}}$	763 Ns/kg
Nose Gear attachment longitudinal position with respect to CG in body axes	$x^{\mathcal{B}}_{\mathcal{S}/\mathcal{B}_{NG}}$	1.41 m
Nose Gear attachment lateral position with respect to CG in body axes	$y^{\mathcal{B}}_{\mathcal{S}/\mathcal{B}_{NG}}$	0 m
Nose Gear attachment vertical position with respect to CG in body axes	$z^{\mathcal{B}}_{\mathcal{S}/\mathcal{B}_{NG}}$	0.37 m
Nose Gear leg assembly mass	m_{NG}	12.9 kg
Nose Gear shock absorber stroke	$\delta_{s_{NG}}$	0.19 m
Nose Gear shock absorber length	$L_{s_{0_{NG}}}$	0.52 m
Nose Gear shock absorber cylinder diameter	$d_{c_{NG}}$	0.030 m
Nose Gear shock absorber orifice diameter	$d_{o_{NG}}$	0.0015 m
Nose Gear shock absorber internal volume	$V_{0_{NG}}$	1.07×10^{-4} m^3
Nose Gear shock absorber preload pressure	$P_{0_{MG}}$	1.8×10^5 Pa
Orifice discharge coefficient	c_d	0.61
Nose Gear tire undeformed radius	$r_{t_{0_{NG}}}$	0.215 m
Nose Gear tire equivalent stiffness coefficient	$k_{t_{NG}}$	5.64×10^5 N/m
Nose Gear tire equivalent damping coefficient	$c_{t_{NG}}$	763 Ns/kg

3. A Procedure for Modeling the Airplane Aerodynamics Based on Semiempirical Methods

The aim of this section is to define a procedure for generating an aircraft aerodynamic database using semi-empirical methodologies. The database should be potentially nonlinear in the flight mechanics parameters, i.e., aerodynamic angles, their derivatives, rates and Mach numbers, and should include all features needed to accurately predict the aerodynamic behavior during terminal maneuvers. Hence, it should consider different configurations (with flaps and gear extended or retracted), the impact of ground effect and different Mach numbers. Clearly, the process requires multiple analyses and the use of semi-empirical methodologies allows the user to obtain the dataset in a couple of minutes, making this tool a valuable option also for preliminary investigations and design optimizations, which can complement traditional simplified approaches [20,21].

Due to certain limitations of the Datcom software, and in particular that only one movable surface can be analyzed at a time, the derivation of the aerodynamic model is performed by simulating multiple analyses in a prescribed process, consisting of seven steps.

Table 4 reports the seven analyses that are performed, the goal of each analysis, and a typical computational time on an off-the-shelf laptop. Each analysis will then be thoroughly described in the forthcoming paragraphs.

Table 4. List of the semiempirical analyses to derive the overall aerodynamic dataset.

#	Elements in the Analysis	Tool	Obtained Sub-Model	Computing Time
1	Entire airplane + Ailerons	Datcom	All stability derivatives aileron control derivatives	60 s
2	Wing + Body + Flap	Datcom	Lift, drag and moment coefficients with and without flaps	100 s
3	Wing + Body + Flap + Ground effect	Datcom	Lift, drag and moment coefficients with and without flaps, in ground effect	30 s

Table 4. *Cont.*

#	Elements in the Analysis	Tool	Obtained Sub-Model	Computing Time
4	Entire airplane + Elevator	Datcom	Elevator impact on lift, drag and moment coefficients	250 s
5	Isolated fuselage (rotated by 90 deg)	Datcom	Drag of the fuselage for different sideslip angles	30 s
6	Isolated landing gear	Ref. [20]	Landing gear drag and pitching moment	0 s
7	Vertical tail and rudder	Ref. [20]	Rudder control derivatives	0 s

3.1. First Analysis: Entire Airplane with Ailerons

The first analysis considers the entire airplane, i.e., fuselage, wing, horizontal and vertical tails, and includes the presence of the ailerons. This step is mainly performed with Datcom through the analysis type, called `wing-body-horizontal tail-vertical tail-ventral fin` in the manual [22].

With this analysis, Datcom provides look-up tables with the entire set of stability derivatives and the aileron control derivatives as functions of different altitudes h and Mach numbers M. In terms of the longitudinal variables, the resulting submodel consists of the coefficients of lift, drag and pitching moment about a reference point G, denoted respectively as $C_L(\alpha,\ M,\ h)$, $C_L(\alpha,\ M,\ h)$ and $C_{\mathcal{M}_G}(\alpha,\ M,\ h)$, the derivatives of lift and moment coefficients with respect to the pitch rate q, $C_{Lq}(\alpha,\ M,\ h)$ and $C_{\mathcal{M}_{Gq}}(\alpha,\ M,\ h)$. Dealing with the lateral-directional variables, the output of this analysis consists of the derivatives of the lateral forces, rolling moment and yawing moment with respect to the sideslip angle β, $C_{Y\beta}(M,\ h)$, $C_{\mathcal{L}_{G\beta}}(\alpha,\ M,\ h)$ and $C_{\mathcal{N}_{G\beta}}(\alpha,\ M,\ h)$, as well as their derivatives with respect to roll and yaw rates p and r, $C_{Yp}(\alpha,\ M,\ h)$, $C_{\mathcal{L}_{Gp}}(\alpha,\ M,\ h)$ and $C_{\mathcal{N}_{Gp}}(M,\ h)$, $C_{Yr}(\alpha,\ M,\ h)$, $C_{\mathcal{L}_{Gr}}(\alpha,\ M,\ h)$ and $C_{\mathcal{N}_{Gr}}(M,\ h)$. Note that the yawing moment derivatives are assumed to be independent of the angle of attack. The aileron control derivatives, $C_{\mathcal{L}_{G\delta_A}}(\delta_A,\ M,\ h)$ and $C_{\mathcal{N}_{G\delta_A}}(\alpha,\ \delta_A\ M,\ h)$, are provided as well.

The stability derivative $C_{Yr}(M,\ h)$, not directly computed by Datcom, is evaluated as

$$C_{Yr}(M,\ h) = -\frac{2\,l_v}{b}\,C_{Y\beta}(M,\ h) \tag{1}$$

where l_v is the distance between the reference point G and the aerodynamic center of the vertical tail, measured along the airplane longitudinal axis.

It is noteworthy that Matlab R2022b has a function, `»datcomimport`, which automatically reads the output files and generates a dedicated structure with all results. Additionally, the aileron control derivatives are also provided. Given the symmetry of the problem, aileron analysis is performed only for positive deflections corresponding to right-aileron-down. Then, estimated control effects are mirrored to obtain the values for negative deflections. As a final remark, notice that to avoid computational issues, the entire set of analyses should be split into multiple sub-analyses.

3.2. Second Analysis: Wing-Body and Flaps

This analysis, aimed specifically at computing the impact of flap deflections on the steady lift, drag and moment coefficients for different Mach numbers and altitudes, is performed in Datcom through the analysis called *Body + Wing* in [22]. The output of this analysis consists of the variation of the lift coefficient at zero angle of attack $\Delta C_L(\delta_F,\ M,\ h)$, where δ_F is the flap deflection, the variation of the maximum lift coefficient $\Delta C_{L_{max}}(\delta_F,\ M,\ h)$, the variation of the minimum drag coefficient $\Delta C_{D_{min}}(\delta_F,\ M,\ h)$ and

induced drag $\Delta C_{D_i}(\alpha,\ \delta_F,\ M,\ h)$, and finally, the variation in pitching moment coefficient $\Delta C^F_{\mathcal{M}}(\delta_F, M, h)$.

All these incremental values must be added to the unflapped values obtained in the first analysis (Section 3.1).

3.3. Third Analysis: Evaluation of Ground Effect

The ground effect analysis is performed in conjunction with flaps. As reported in [22], ground effect is essentially negligible for ground heights greater than the wingspan b. The analysis consists of computing the steady lift, drag and pitching moment coefficients for every combination of flap deflection and ground height.

Although the literature recognizes that ground effect may significantly influence lateral-directional derivatives [23], Datcom does not include any corrections to lateral-directional derivatives.

It is worth noting that the native Matlab function `»datcomimport` does not properly read the Datcom output files for ground effect analyses, and consequently, a dedicated function was created.

Figure 2 shows some examples of the variation of the polar data with flaps and ground effect: Each subplot refers to a different flap deflection (left plot $\delta_F = 0$, center plot $\delta_F = 15$ deg and right plot $\delta_F = 40$ deg), whereas each line in the plot refers to the specific height as indicated in the legend.

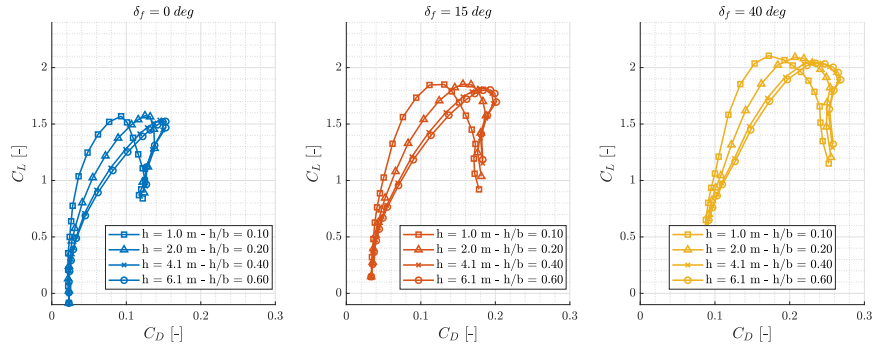

(**a**) Polar data for different flap deflections and ground distances.

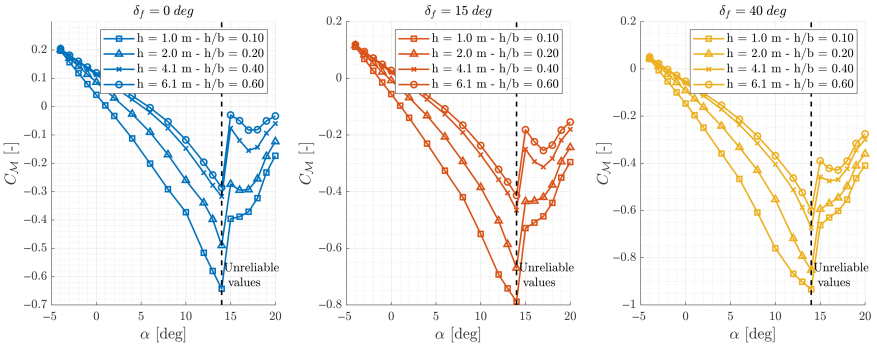

(**b**) Pitching moment coefficient for different flap deflections and ground distances.

Figure 2. Ground effect on polar and pitching moment coefficient, for different flap deflections.

It can be observed that all curves tend to overlap for h/b values close to 0.6, indicating that for h/b between 0.7 and 1, the ground effect is negligible. In the polar data, displayed in the upper plots, the reduction in the drag coefficient for a given lift due to ground proximity is evident as is a mild increase in the maximum lift coefficient. Additionally, a crucial aspect that can be observed in the behavior of the pitching moment is the pitch-down effect caused by ground effect. A similar effect on pitching moment was also noted in Ref. [24] for a larger transport aircraft, the Comet 3B. Additionally, the modeling approach predicts a

mild reduction in the stall angle of attack due to ground effect, which is not shown here for the sake of brevity. This indication is consistent with practical stall testing experience [25].

Furthermore, Figure 2 allows a basic but important validation of the polar data concerning the maximum lift coefficients. Ref. [26] provides specification data for the Navion airplane, including the maximum takeoff weight of 12,677 kN and the stall speed in clean configuration, equal to 27.7 m/s, and in landing configuration, equal to 24.14 m/s. Such indications yield, via straightforward computations, the values of the maximum lift coefficients in clean and landing configurations, respectively equal to 1.57 and 2.07. Both values are perfectly matched by the Datcom estimation as visible in the polar data with null and 40 deg flap deflection (Figure 2, up-left and up-right plots).

3.4. Fourth Analysis: Entire Airplane and Elevator

The elevator is treated by Datcom as a flap positioned on the horizontal tail. Similar to the second analysis (Section 3.2), this analysis allows one to obtain the variation in lift, drag and moment coefficients as functions of the angle of attack α, Mach number M, altitude h and elevator deflection δ_E. In particular, the variation in lift coefficient and in its maximum value are indicated as $\Delta C_L(\delta_E,\ M,\ h)$ and $\Delta C_{L_{max}}(\delta_E,\ M,\ h)$, the variation in minimum drag and induced drag as $\Delta C_{D_{min}}(\delta_E, M, h)$ and $\Delta C_{D_i}(\alpha, \delta_E, M, h)$, and the variation in the pitching moment coefficient as $\Delta C^E_{\mathcal{M}_G}(\delta_E, M, h)$.

3.5. Fifth Analysis: Isolated Fuselage

In order to estimate the increase in the drag due to the sideslip angle, an analysis of the isolated fuselage is performed. Since Datcom does not support analyses with variable β, to obtain the desired drag increment $\Delta C_{D_{fus}}(\beta)$, one may define a 90-degree rotated fuselage in Datcom, as shown in Figure 3. In this configuration, the simulated angle of attack represents the physical sideslip angle. Consequently, the analysis for varying α, which in Datcom is called `Body` alone, gives the drag coefficient of the fuselage as a function of the physical sideslip angle.

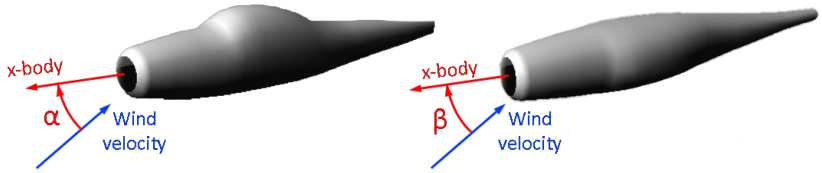

Figure 3. Fuselage rotation in Datcom to obtain $\Delta C_{D_{fus}}(\beta)$.

Once the drag coefficient of the rotated fuselage $C_{D_{fus}}(\beta)$ is obtained, the specific increase due to the sole variation of β, denoted as $\Delta C_{D_{fus}}(\beta)$, is computed by subtracting the value of the fuselage drag at null sideslip, as $\Delta C_{D_{fus}}(\beta) = C_{D_{fus}}(\beta) - C_{D_{fus}}(0)$. Figure 4 illustrates the resulting $\Delta C_{D_{fus}}(\beta)$ function, where it is possible to notice that the impact of the fuselage lateral misalignment on the drag coefficient rapidly becomes significant for sideslip angles greater than 10 deg.

It is important to note that the rotated fuselage is not exactly identical to the original body, as the rotated one exhibits an additional symmetry with respect to the physical $x - y$ plane, which does not exist in the original configuration. Consequently, the geometric model of the fuselage is not physically accurate but still preserves the overall dimensions. The resulting drag function $\Delta C_{D_{fus}}(\beta)$, although affected by this discrepancy, provides for a good approximation of the impact of sideslip angles on the overall drag.

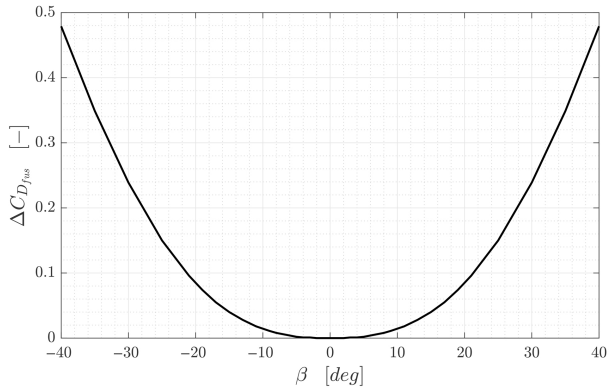

Figure 4. Drag coefficient increment due to fuselage misalignment with airspeed.

3.6. Sixth and Seventh Analyses: Landing Gear Drag and Rudder Control Derivatives

In the previous analyses, there are still some significant aerodynamic characteristics to be evaluated. Specifically, the lateral force derivative with respect to the rudder deflection $C_{Y_{\delta_R}}$ is computed using the classical Roskam estimation procedure ([20], pt. VI, Section 6) while $C_{\mathcal{L}_{\delta_R}}$ and $C_{\mathcal{N}_{\delta_R}}$ are estimated as follows:

$$C_{\mathcal{L}_{\delta_R}}(Ma) = \frac{z_v}{b} C_{Y_{\delta_R}}(Ma) \tag{2a}$$

$$C_{\mathcal{N}_{\delta_R}}(Ma) = -\frac{l_v}{b} C_{Y_{\delta_R}}(Ma) \tag{2b}$$

where z_v and l_v are the vertical and longitudinal distances between the center of gravity and the aerodynamic center of the vertical tail.

The nose and main landing gears are aerodynamically characterized by an additional contribution to the parasite drag and pitching moment coefficients, following the Roskam procedure [27]. For the reference aircraft, the parasite drag is estimated as

$$C_{Dgear}(\delta_G) = 0.0148 \cdot \delta_G, \qquad \delta_G \in [0, 1] \tag{3}$$

where δ_G, a variable representing the landing gear position, is equal to 1 when the gear is fully deployed and 0 when retracted. Assuming that the vertical position of the application point of the resultant of the landing gear frictional and pressure force distributions is located at the center of the main landing gear wheel, the pitching moment coefficient due to the landing gear can be evaluated as

$$C_{\mathcal{M}_{G\,gear}}(\delta_G) = -\frac{z_G}{c} C_{Dgear}(\delta_G) \tag{4}$$

where z_G is the distance between the aircraft center of gravity and the main gear wheels.

3.7. Overall Aerodynamic Model

In the previous sections, from Sections 3.1–3.6, all contributions to the overall airplane aerodynamic model were computed, yielding a series of look-up tables depending on the most important flight mechanics variables. All these look-up tables should now be combined and integrated into the simulation environment.

The lift coefficient is expressed as

$$C_L(\alpha, M, h, \delta_F, \delta_E, q, \dot{\alpha}) = \mathcal{F}_{L\alpha}(\alpha, M, h) + \mathcal{F}_{Lh}(\alpha, h, \delta_F) + \\ + \mathcal{F}_{LF}(\alpha, M, h, \delta_F) + \mathcal{F}_{LE}(\alpha, M, h, \delta_E) + \\ + C_{L_q}(M, h)\,\frac{c}{2V_{TAS}}\,q + C_{L_{\dot{\alpha}}}(\alpha, M, h)\,\frac{c}{2V_{TAS}}\,\dot{\alpha}. \quad (5)$$

The look-up table $\mathcal{F}_{L\alpha}(\alpha, M, h)$ represents the static lift coefficient computed in the first analysis, Section 3.1, that considers the entire aircraft excluding the movable surfaces.

The look-up table $\mathcal{F}_{Lh}(\alpha, h, \delta_F)$ corresponds to the variation in the static lift coefficient due to the ground effect, as it is computed in the third analysis and described in Section 3.3. The dependence on δ_F stresses the fact that the ground effect may be slightly different for different flap deflections, as pointed out in Section 3.3.

Furthermore, the look-up tables $\mathcal{F}_{LF}(\alpha, M, h, \delta_F)$ and $\mathcal{F}_{LE}(\alpha, M, h, \delta_E)$ consider the variation in the static lift coefficient due to the flap and elevator deflection, respectively, as extracted from the analyses described in Sections 3.2 and 3.4. In both cases, Datcom provides the variation in the coefficient at the null and maximum angles of attack, indicated respectively with $\Delta C_{L,max\,F}(\delta_F, M, h)$ and $\Delta C_{LF}(\delta_F, M, h)$ for flap deflection and with $\Delta C_{L,max\,E}(\delta_E, M, h)$ and $\Delta C_{LE}(\delta_E, M, h)$ for elevator deflection. For a generic α, the lift coefficient can be evaluated by interpolating between the two values as

$$\mathcal{F}_{LF}(\alpha, M, h, \delta_F) = \frac{\Delta C_{L,max}(\delta_F, M, h)}{\alpha_{C_{L,max}}(M, h)}\,\alpha + \frac{\Delta C_L(\delta_F, M, h)}{\alpha_{C_{L,max}}(M, h)}\,(\alpha_{C_{L,max}}(M, h) - \alpha) \quad (6)$$

and

$$\mathcal{F}_{LE}(\alpha, M, h, \delta_E) = \frac{\Delta C_{L,max}(\delta_E, M, h)}{\alpha_{C_{L,max}}(M, h)}\,\alpha + \frac{\Delta C_L(\delta_E, M, h)}{\alpha_{C_{L,max}}(M, h)}\,(\alpha_{C_{L,max}}(M, h) - \alpha). \quad (7)$$

Finally, the dimensionless coefficients $C_{L_q}(M, h)$ and $C_{L_{\dot{\alpha}}}(\alpha, Ma, h)$ are the derivatives of the lift coefficient with respect to the pitch rate and to the variation of the angle of attack, which are directly provided by Datcom, as outputs of the first analysis, Section 3.1.

The drag coefficient is expressed as

$$C_D(\alpha, \beta, M, h, \delta_F, \delta_E, \delta_G) = \mathcal{F}_{D\alpha}(\alpha, M, h) + \mathcal{F}_{Dh}(\alpha, h, \delta_F) + \\ + \mathcal{F}_{DF}(\alpha, M, h, \delta_F) + \mathcal{F}_{DE}(\alpha, M, h, \delta_E) + \\ + \Delta C_{D_{fus}}(\beta, M, h) + C_{D_{gear}}(\delta_G) \quad (8)$$

Function $\mathcal{F}_{D\alpha}(\alpha, M, h)$ represents the look-up table of the C_D of the whole aircraft (wing, fuselage and empannges) obtained through the first analysis, Section 3.1. Look-up table $\mathcal{F}_{Dh}(\alpha, h, \delta_F)$ includes the impact of the ground effect that depends also on flap deflection obtained from the analysis in Section 3.3. Tables $\mathcal{F}_{DF}(\alpha, M, h, \delta_F)$ and $\mathcal{F}_{DE}(\alpha, M, h, \delta_E)$ include the increase in drag coefficient due to flap deflection and elevator deflection, respectively, as described in Sections 3.2 and 3.4. For flap analysis, the increases in minimum $\Delta C_{D_{min\,F}}(\delta_F, M, h)$ and induced $\Delta C_{D_{i\,F}}(\alpha, \delta_F, M, h)$ drag are available and allow for the quantification of the flap impact on drag as

$$\mathcal{F}_{DF}(\alpha, M, h, \delta_F) = \Delta C_{D_{min\,F}}(\delta_F, M, h) + \Delta C_{D_{i\,F}}(\alpha, \delta_F, M, h). \quad (9)$$

The elevator impact is evaluated in the same way as

$$\mathcal{F}_{DE}(\alpha, M, h, \delta_E) = \Delta C_{D_{min\,E}}(\delta_E, M, h) + \Delta C_{D_{i\,E}}(\alpha, \delta_E, M, h). \quad (10)$$

Here, $\Delta C_{D_{min\,E}}(\delta_E, M, h)$ and $\Delta C_{D_{i\,E}}(\alpha, \delta_E, M, h)$ are the increases in minimum and induced drag coefficients due to elevator deflection.

Finally, $\Delta C_{D_{fus}}(\beta, M, h)$ represents the look-up table describing the increase in the drag coefficient due to the fuselage operating in misaligned conditions, as described in Section 3.5, whereas $C_{Dgear}(\delta_G)$ is the drag increase due to the extension of the landing gear, depending on its position δ_G with null value associated with retracted and 1 with fully extended landing gear, as described in Section 3.6.

To obtain the longitudinal and vertical load coefficients, i.e., the body force coefficients, the usual relationships are used:

$$C_X = +C_L \sin\alpha - C_D \cos\alpha, \tag{11a}$$

$$C_Z = -C_L \cos\alpha - C_D \sin\alpha. \tag{11b}$$

The pitching moment coefficient is formulated as

$$\begin{aligned} C_{\mathcal{M}_G}(\alpha, M, h, \delta_F, \delta_E, \delta_G, q, \dot{\alpha}) = {} & \mathcal{F}_{\mathcal{M}\alpha}(\alpha, M, h) + \mathcal{F}_{\mathcal{M}h}(\alpha, h, \delta_F) + \Delta C^F_{\mathcal{M}}(\delta_F, M, h) + \\ & + \Delta C^E_{\mathcal{M}}(\delta_E, M, h) + C_{\mathcal{M}_q}(M, h)\,\frac{c}{2V_{TAS}}\,q + \\ & + C_{\mathcal{M}_{\dot{\alpha}}}(\alpha, M, h)\,\frac{c}{2V_{TAS}}\,\dot{\alpha} + C_{\mathcal{M}gear}(\delta_G), \end{aligned} \tag{12}$$

where $\mathcal{F}_{\mathcal{M}\alpha}$ and $\mathcal{F}_{\mathcal{M}h}$ are the look-up tables for the pitching moment of the whole airplane (wing, fuselage, and empennages) in free air and ground effect, respectively, derived from Sections 3.1 and 3.3, the latter also dependent on flap deflection δ_F. The modification of the pitching moment coefficient due to flap and elevator deflections is captured by the look-up table $\Delta C^F_{\mathcal{M}}(\delta_F, M, h)$ and $\Delta C^E_{\mathcal{M}}(\delta_E, M, h)$, obtained from analysis in Sections 3.2 and 3.4. $C_{\mathcal{M}_q}(M, h)$ and $C_{\mathcal{M}_{\dot{\alpha}}}(\alpha, M, h)$ are the derivatives of the pitching moment coefficient with respect to the pitch rate and to the angle of attack acceleration, respectively, both estimated in the first analysis, Section 3.1.

The side force coefficient, C_Y, is formulated as

$$\begin{aligned} C_Y(\alpha, \beta, Ma, h, p, r, \delta_R) = {} & C_{Y_\beta}(M, h)\,\beta + C_{Y_p}(\alpha, M, h)\,\frac{b}{2V_{TAS}}\,p + \\ & + C_{Y_r}(M, h)\,\frac{b}{2V_{TAS}}\,r + C_{Y_{\delta_R}}(M)\,\delta_R. \end{aligned} \tag{13}$$

Look-up tables $C_{Y_\beta}(Ma, h)$ and $C_{Y_p}(\alpha, M, h)$ and $C_{Y_r}(M, h)$ represent the derivatives of the lateral force coefficient with respect to the sideslip angle and pitch rate, obtained from Section 3.1. The look-up table $C_{Y_r}(Ma, h)$, as seen in Section 3, is evaluated from C_{Y_β}, as in Equation (1). The rudder-side-force control derivative $C_{Y_{\delta_R}}(Ma)$ is computed using Roskam method, as described in Section 3.6. Finally, $C_{\mathcal{M}gear}(\delta_G)$ represents the contribution to the aircraft pitching moment due to the landing gear.

The rolling moment coefficient, $C_{\mathcal{L}_G}$, is formulated as

$$\begin{aligned} C_{\mathcal{L}_G}(\alpha, \beta, M, h, p, r, \delta_A, \delta_R) = {} & C_{\mathcal{L}_{G\beta}}(\alpha, M, h)\,\beta + C_{\mathcal{L}_{G_p}}(\alpha, M, h)\,\frac{b}{2V_{TAS}}\,p + \\ & + C_{\mathcal{L}_{G_r}}(\alpha, M, h)\,\frac{b}{2V_{TAS}}\,r + C_{\mathcal{L}_G}\Big|_{\delta_A}(\delta_A, M, h) + C_{\mathcal{L}_{G\delta_R}}(M)\,\delta_R. \end{aligned} \tag{14}$$

The look-up table $C_{\mathcal{L}_{G\delta_R}}(Ma)$, representing the rudder control derivative, is computed through Equation (2a). The other contributions, i.e., the lateral stability $C_{\mathcal{L}_{G\beta}}(\alpha, M, h)$, the damping in roll $C_{\mathcal{L}_{G_p}}(\alpha, M, h)$, the roll-due-to-yaw derivative $C_{\mathcal{L}_{G_r}}(\alpha, M, h)$ and

the aileron control derivative $C_{\mathcal{L}_G}|_{\delta_A}(\delta_A, M, h)$, are computed through the analysis in Section 3.1.

Similarly, the yawing moment coefficient $C_{\mathcal{N}_G}$ is modeled as

$$C_{\mathcal{N}_G}(\alpha, \beta, Ma, h, p, r, \delta_A, \delta_R) = C_{\mathcal{N}_{G\beta}}(Ma, h)\,\beta + C_{\mathcal{N}_{Gp}}(\alpha, Ma, h)\,\frac{b}{2V_{TAS}}\,p + \\ + C_{\mathcal{N}_{Gr}}(\alpha, Ma, h)\,\frac{b}{2V_{TAS}}\,r + C_{\mathcal{N}_G}\Big|_{\delta_A}(\alpha, \delta_A, Ma, h) + C_{\mathcal{N}_{G\delta_R}}(Ma)\,\delta_R, \tag{15}$$

where the rudder control derivative $C_{\mathcal{N}_{\delta_R}}(Ma)$ is evaluated through Equation (2b), while the directional derivative $C_{\mathcal{N}_{G\beta}}(Ma, h)$, the yawing-due-to-roll derivative $C_{\mathcal{N}_{Gp}}(\alpha, Ma, h)$, the damping in yaw $C_{\mathcal{N}_{Gr}}(\alpha, Ma, h)$ and the cross-coupling effect of the aileron deflection on the yawing moment coefficient $C_{\mathcal{N}_G}|_{\delta_A}(\alpha, \delta_A, Ma, h)$ are obtained through the first analysis, Section 3.1.

Finally, the components of aerodynamic and propulsive loads in the body reference frame are expressed as

$$X = q_D\,S\,C_X + C_{X_{\delta_T}}\,\delta_T \tag{16a}$$

$$Y = q_D\,S\,C_Y \tag{16b}$$

$$Z = q_D\,S\,C_Z + C_{Z_{\delta_T}}\,\delta_T \tag{16c}$$

$$\mathcal{L}_G = q_D\,S\,b\,C_{\mathcal{L}_G} \tag{16d}$$

$$\mathcal{M}_G = q_D\,S\,c\,C_{\mathcal{M}_G} + C_{\mathcal{M}_{G\delta_T}}\,\delta_T \tag{16e}$$

$$\mathcal{N}_G = q_D\,S\,b\,C_{\mathcal{N}_G} \tag{16f}$$

where q_D is the dynamic pressure, S the wing area, c the mean aerodynamic chord and b the wingspan. Since the thrust in the Navion is considered aligned with the body longitudinal x-axis, $C_{X_{\delta_T}}$ is set to 1, and $C_{Z_{\delta_T}}$ to 0. Hence, δ_T corresponds exactly to the thrust value. Similarly, the coefficient $C_{\mathcal{M}_{G\delta_T}}$, which accounts for the pitching moment contribution due to thrust, is set to zero. Additionally, any thrust effect on the lateral-directional loads is considered null.

The entire aerodynamic database of the reference airplane, generated through the present process, is available in an online repository [28].

4. Simulation Environment

The simulator, capable of handling the entire flight, including terminal maneuvers (i.e., between the pre-flight and post-flight stationary ground conditions), is an evolution of the one described in [15]. It relies on standard rigid-body dynamics equations for the airplane motion. Cardan angles are used to parameterize the orientation of the airframe with respect to the navigational frame, while the aerodynamic angles are calculated taking into account the presence of wind with a specified magnitude and direction.

The dynamics of landing gears, including shock absorber strokes and tire deformations, complementing the rigid-body dynamics, are activated by a specialized function that detects which leg, if any, has made contact with the ground. Specifically, a simplified tricycle landing gear geometry, consisting of a tire and an oleo-pneumatic shock absorber, is considered. Tire behavior is rendered through a point-contact model, represented by a linear spring-damper system. The values of the equivalent tire spring and damper characteristics are chosen from the literature to yield realistic deformations during simulations. The shock absorbers are modeled using the usual physical nonlinear equations linking the elastic force to the stroke and the pressure inside the absorber gas chamber, whereas the dissipative

component is modeled through the damping arising from the flow of the oil through an equivalent orifice.

Friction between tires and ground is formulated according to [10], which provides a suitable formulation for longitudinal and lateral friction coefficients. Braking is simulated as an additional friction force.

The forces generated at each landing gear contact point are integrated into the overall equations of motion of the aircraft, along with the aeropropulsive forces computed through the process described in Section 3.

The entire virtual model, including both the airplane rigid body dynamics, the dynamics of the shock absorbers and tires, results in a stiff problem, primarily because of the landing gear dynamics. To cope with that, the system was simulated using the variable-step integrator implemented in the Matlab [29] function `ode15s`, tailored for stiff systems.

Whenever a contact or impact event (i.e., a leg touching or lifting-off the ground) is detected, the system dynamics and the number of states must be modified. To handle such discontinuities, the simulation is broken into a variable number of sub-simulations: The simulation is halted and restarted, modifying the state variables and the system dynamics when an event is detected.

The entire mathematical formulation is reported in [15] and is not part of the present paper.

To allow for a complete simulation of the terminal maneuvers, the simulator is here complemented with a simplified model of the pilot, rendered as a controller acting on the commanded inputs to follow prescribed flight trajectories. In particular, three controllers has been implemented. The first considers a deflection of the elevator to maintain a certain descent velocity during the approach in landing simulations; the second considers a thrust control to maintain the flight speed, again during landing; finally, a nose wheel steer control is used to maintain the runway after touchdown. The first two controls are inspired by Ref. [30].

The control applied to the descent speed follows a simple proportional relationship:

$$\delta_E(t) = \delta_{E_{trim}} + K_{V_D}(V_D(t) - V_{D_{ref}}(t)) \tag{17}$$

where $\delta_{E_{trim}}$ is the elevator deflection in the approach phase, K_{V_D} is the proportional gain and $V_D(t)$ is the actual descent speed and $V_{D_{ref}}(t)$ is the desired one.

In order to maintain a constant V_{TAS}, the throttle is set according to this controller:

$$\delta_T(t) = \delta_{T_{trim}} + K_{V_{TAS}}(V_{TAS}(t) - V_{TAS_{trim}}) \tag{18}$$

where $\delta_{T_{trim}}$ is the throttle in the approach phase and $V_{TAS}(t)$ and $V_{TAS_{trim}}$ represent the actual flight speed and the desired one.

The proportional gains K_{V_D} and $K_{V_{TAS}}$ were set using a trial and error approach.

With the goal of increasing the robustness against possible changes in pitching moment due to the ground effect, it is possible to include an additional term proportional to the pitch rate or to the ground distance in the elevator control law.

The steering control is designed to maintain the airplane trajectory on the ground, after landing, parallel to the runway direction. To this end, the angle σ, representing the nose wheel rotation (positive to the right), is formulated as

$$\sigma = K_\psi(\psi - \chi_{\text{runway}}) + K_y \Delta y_{CG} \tag{19}$$

where ψ is the airplane heading angle, χ_{runway} is the runway direction and Δy_{CG} is the lateral deviation of the airplane center of gravity from the runway centerline. The control gains K_ψ and K_y are again set through a trial and error approach.

5. Results

In this section, different simulation tests are presented, with the goal of showing the features of the developed tool and studying landing performance as a function of several parameters. At first, in Section 5.1, an example of a takeoff is presented. Then, Section 5.2 deals with the landing simulations. Finally, a parametric analysis of landing for different values of the approach speed and the crosswind velocity is performed and reported in Section 6.

5.1. Takeoff Simulations

An example of a takeoff simulation in calm air is now presented. The simulation is realistic and includes the retraction of both the landing gear and the flaps. The airplane starts at rest on the ground and accelerates following the throttle control similar to that of Equation (18):

$$\delta_T(t) = min\{4000\ N,\ \ K_{V_{TAS}} \cdot (V_{TAS}(t) - V_{TAS_{ref}})\} \tag{20}$$

where $V_{TAS_{ref}} = 50$ m/s and $\delta_{T\text{MAX}} = 4000$ N. The maximum thrust $\delta_{T\text{MAX}}$ was set to obtain a ground roll similar to that reported in [26].

The ground acceleration continues until the airplane reaches the rotation speed V_R equal to 35 m/s, when the elevator control is imposed according to the rule based on Equation (21):

$$\delta_E(t) = \begin{cases} 0\ deg, & \text{if } V_{TAS}(t) \le V_R \\ K_{V_D} \cdot (V_D(t) - V_{D_{ref}}) + \delta_{E_{trim}}, & \text{if } V_{TAS}(t) > V_R \end{cases} \tag{21}$$

where $V_{D_{ref}}$ is -4.2 m/s corresponding to a rate of climb equal to 830 fpm). $\delta_{E_{trim}}$ was set equal to 4.1 deg, a value that, according to the aerodynamic model, corresponds to the deflection for trimming the airplane at speed equal to 50 m/s, with a climb rate of 4.2 m/s, in clean configuration, i.e., with both gear and flaps retracted.

Landing gear δ_G and flap δ_F retractions were defined as

$$\delta_G(t) = \begin{cases} 1, & \text{if } t \le t_{50\text{m}} \\ 1 - \frac{t - t_{50\text{m}}}{5\text{ s}}, & \text{if } t_{50\text{m}} < t < t_{50\text{m}} + 5\text{ s} \\ 0, & \text{if } t \ge t_{50\text{m}} + 5\text{ s} \end{cases} \tag{22}$$

$$\delta_F(t) = \begin{cases} 15\text{ deg}, & \text{if } t \le t_{90\text{m}} \\ 15\text{ deg} - \frac{15\text{ deg}}{5\text{ s}}(t - t_{90\text{m}}), & \text{if } t_{90\text{m}} < t < t_{90\text{m}} + 5\text{ s} \\ 0\text{ deg}, & \text{if } t \ge t_{90\text{m}} + 5\text{ s} \end{cases} \tag{23}$$

where $t_{50\text{m}}$ and $t_{90\text{m}}$ refer to the time instants where the airplane center of gravity respectively reaches the altitude of 50 m and 90 m. The time to retract the landing gear from its full-extended, $\delta_G = 1$, to full-retracted, $\delta_G = 0$, position was set to a reasonable value, here chosen as 5 s. The same value was also selected as the time to retract the flaps.

Figure 5 shows the resulting time histories of landing gear and flap positions.

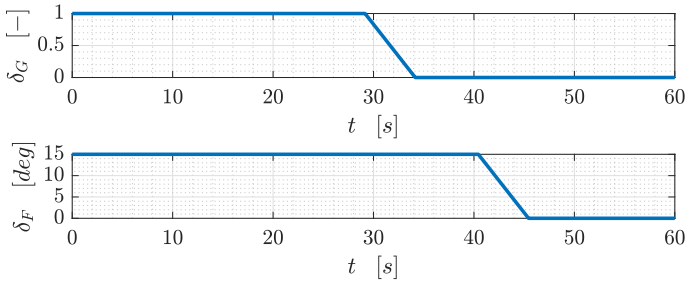

Figure 5. Landing gear position and flaps deflection during takeoff.

The resulting elevator deflection and the thrust are shown in Figure 6, along with the feedback variables V_D and V_{TAS}.

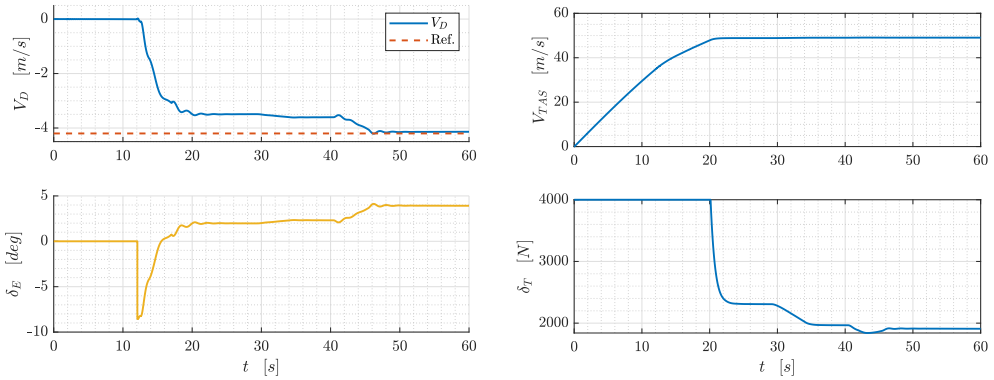

(**a**) Vertical speed and elevator deflection (**b**) Airspeed and thrust

Figure 6. Time histories of control input and feedback variables during takeoff.

Figure 7 shows the time histories of the trajectory, aerodynamic and Euler angles, while the deformations of the landing gear are shown in Figure 8.

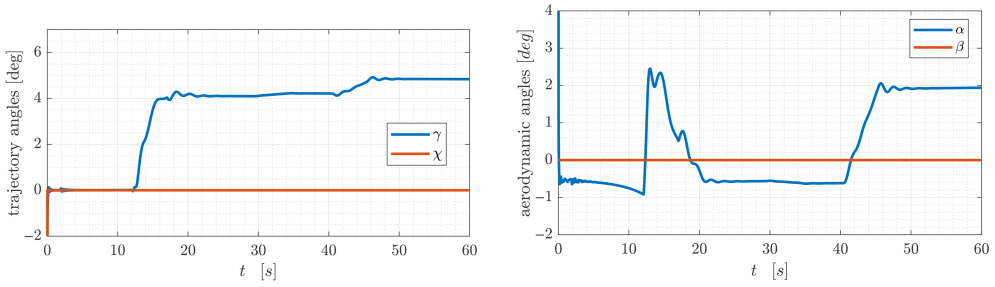

(**a**) Trajectory angles (**b**) Aerodynamic angles

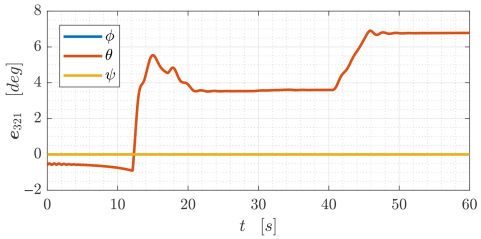

(**c**) Euler angles (roll ϕ and heading ψ angles are both null)

Figure 7. Trajectory, aerodynamic and Euler angles during takeoff.

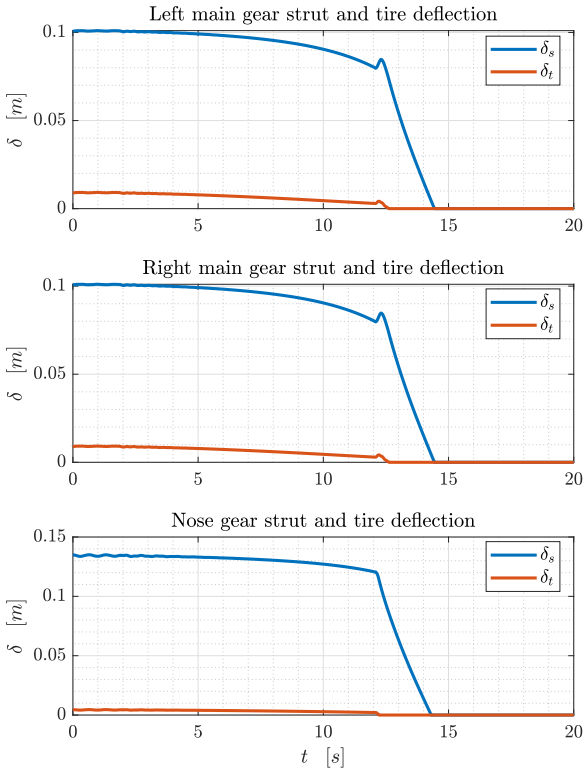

Figure 8. Landing gear deformations during takeoff.

Looking at Figure 8, it is possible to notice that tire and strut deformations decrease as the aircraft accelerates along the runway due to the increase in airplane lift. Additionally, small oscillations are present in the initial instants due to initial conditions that do not exactly correspond to airplane equilibrium on the ground.

From the plots, it is possible to distinguish the different phases of the takeoff that are managed within a single model. In particular, discontinuities present in all plots correspond to changes in the airplane configurations and the lift-off events.

From second 0 to 12, the airplane accelerates on the ground, then the elevator input to lift-off occurs at t = 12 s, when the true airspeed reaches 35 m/s, as in Figure 6. At the same time, as in Figure 8, the nose gear lifts off the ground and its tire deformation becomes zero, while the absorber stroke takes longer to return to the nominal position due to its damping. Immediately after the nose wheel lifts, its normal reaction, no longer balanced by the lift, is transferred to the main landing gear, causing a small increase in the deformation of the struts. At second 20, the desired speed is reached and the thrust is reduced.

Just before $t = 30$ s, the landing gear retraction begins. Its contribution to the pitching moment gradually disappears and the aircraft settles into a new equilibrium configuration, characterized by a slightly different elevator deflection and a lower thrust, as appreciable from Figure 6b. Shortly after $t = 40$ s, the flaps retraction starts and both elevator deflection and thrust are adjusted to follow the prescribed path, causing a significant variation in the angle of attack and pitch angle, as in Figure 7. At the end of the simulation, the airplane is trimmed in the desired climbing flight.

5.2. Landing Simulations

In order to show the importance of a good characterization of the ground effect, two cases were simulated, one including the variation in the airplane aerodynamics due to the ground effect and the other considering constant aerodynamic coefficients regardless of the ground proximity. To isolate the ground effect impact, the analyses are conducted in calm air and without performing a flare maneuver, i.e., fixing elevator, aileron, rudder and

thrust inputs. Without flare, the simulations are not realistic but are still useful to evaluate the impact of the ground effect in terms of the landing performance. The initial conditions for both cases are listed in Table 5.

Table 5. Initial condition for landing simulations.

Parameter	Symbol	Value
Initial airplane height	h_0	15 m
Airspeed	V_{TAS}	30 m/s
Track angle and runway direction	$\chi, \chi_{\text{runway}}$	0 deg
Heading angle	ϕ_{trim}	0 deg
Descent angle	γ_d	1 deg
Flaps deflection	δ_F	40 deg
Landing gear position	δ_G	Full down
Wind speed	v_W	0 m/s (calm air)

Figure 9 shows the output of these simulations, in terms of the airplane trajectory (top plot) and flight angles (bottom plot) as functions of the horizontal location of the airplane center of gravity, $x_C G^{\mathcal{N}}$. The plots compare the case where the ground effect is considered (solid lines) with that where it is not (dashed lines). As clearly seen from the plot, due to the combined modification of the aerodynamics of the wing and tail, the overall aerodynamic pitch moment increases in magnitude while the airplane descends, causing a tendency to pitch down the airplane nose, and the airplane touches the gound with a descent angle of about 3 deg. Such an effect does not always happen, as it is airplane-specific and dependent on the location of the center of gravity and wing aerodynamic center. However, this is a behavior already observed on the de Havilland DH.106 Comet [24].

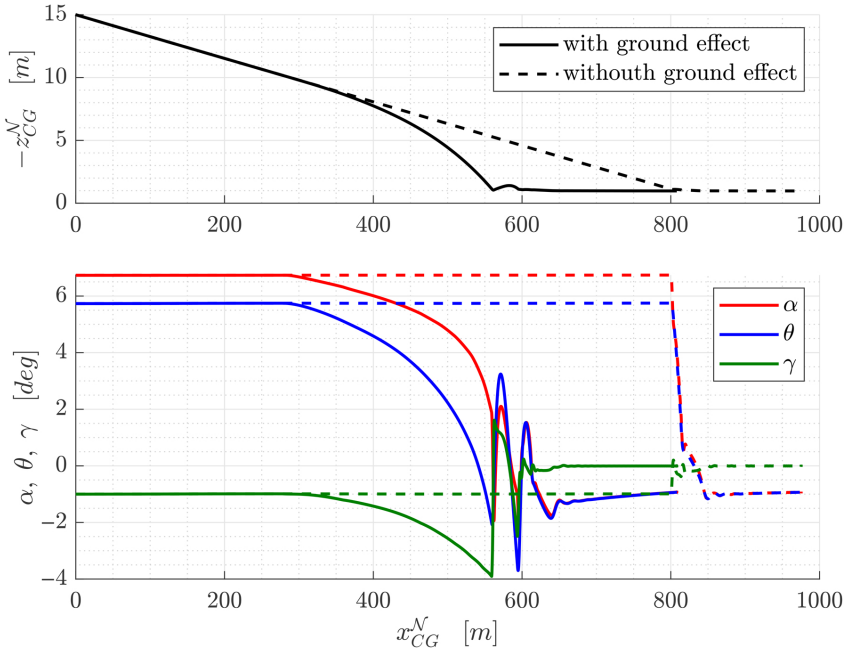

Figure 9. Example of the effect of ground effect on a landing simulation in calm air. Top plot: aircraft trajectory. Bottom plot: pitch angle (green line), climb angle (red line) and angle of attack (blue line). Solid lines refer to the simulation including ground effect, while dashed lines refer to that without ground effect.

5.3. Landing in Crosswind Conditions

In this section, a landing maneuver under crosswind conditions is presented. Specifically, the sideslipped method will be considered, in which the approach is performed

by aligning the airplane heading with the runway orientation, leading to a misaligned descent. In this condition, the wing is not level and the upwind landing gear touches the ground first.

Table 6 reports the initial conditions of the simulation. The components of the wind velocity in the navigational frame are

$$\boldsymbol{v}_{\mathrm{W}}^{\mathcal{N}} = (v_{\mathrm{WN}}, v_{\mathrm{WE}}, v_{\mathrm{WD}})^T = (0, 8, 0)^T \,\mathrm{m/s} \tag{24}$$

with v_{WN} and v_{WE}, respectively, being the northward and eastward wind components, and v_{WD} being the vertical component positive if downward.

Table 6. Initial conditions for landing in crosswind conditions.

Parameter	Symbol	Value
Initial airplane height	h_0	30 m
Airspeed	V_{TAS}	35 m/s
Heading angle	ψ_{trim}	0 deg
Track angle and runway direction	χ, χ_{runway}	0 deg
Descent angle	γ_d	3 deg
Flaps deflection	δ_F	40 deg
Landing gear position	δ_G	1 (down)
Northward wind component	v_{WN}	0 m/s
Eastward wind component	v_{WE}	8 m/s
Vertical wind component	v_{WD}	0 m/s

The wind is maintained constant throughout the entire simulation but the actual wind component felt in the body reference frame can vary according to the orientation of the airplane at each instant of time. In the initial state, since the runway orientation is towards the North and the airplane heading is aligned with the runway, the wind, defined in Equation (24), represents a classical crosswind situation.

The aileron and rudder deflections are maintained constant at their trim positions throughout the simulation, while δ_T, δ_E and the steering of the nose wheel are configured based on the control logic that emulates pilot actions, as described in Section 4.

Aircraft trajectory for the sideslip landing with the steering control is represented in Figure 10, where it is possible to appreciate the trace of the airplane on the ground, mainly resulting from the lateral forces due to crosswind and the nose wheel steering: The aircraft stays close to the runway center without skidding out.

The steering variable σ is shown in Figure 11 (bottom plot), along with the heading angle ψ (top plot) and the lateral location of the airplane center of gravity with respect to the runway centerline $y_{CG}^{\mathcal{N}}$ (middle plot). The action of the steer is able to make the airplane follow both the runway direction and its center line, producing the ground trajectory that was already visualized in Figure 10. The maximum lateral excursion of the center of gravity with respect to the runway centerline results in about 2.5 m, a reasonable value for the aircraft considered in this work.

Airplane body-framed speed components are displayed in Figure 12, where it is possible to notice the impact of the flare on the vertical component W (15–21 s), the effect of the asymmetric touchdown and nose steering on lateral component V (21–30 s) and the effect of brakes on the airplane speed, especially on the longitudinal component U. The landing ends at second 35, about 14 s after the first contact with the ground with the left main gear.

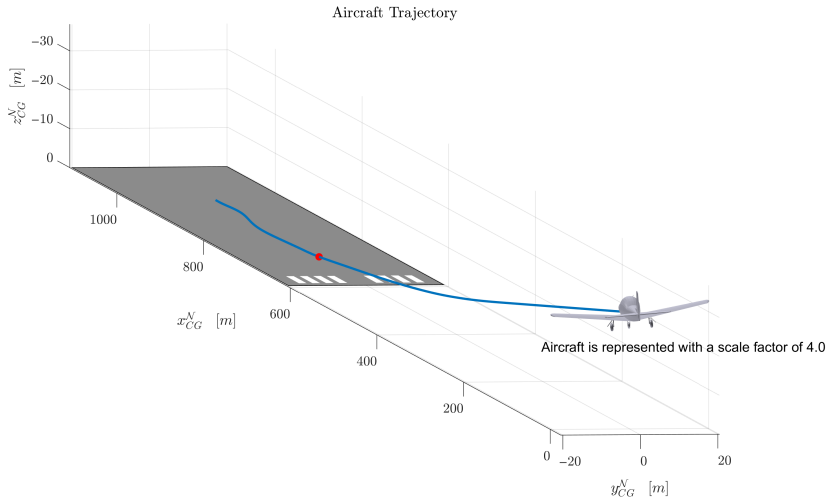

Figure 10. Aircraft trajectory in the sideslip landing, with the steering of the nose wheel. The red marker on the runway indicates the touchdown point.

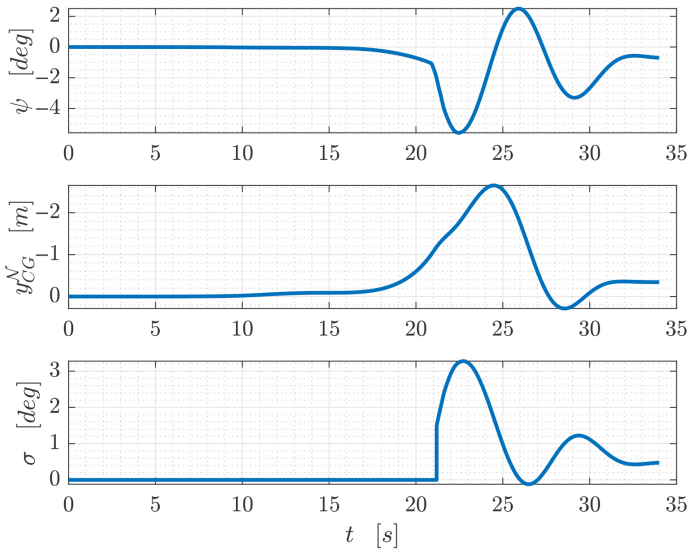

Figure 11. Nose wheel steering control in the sideslip landing: control variable σ and controlled variables ψ and $y_{CG}^{\mathcal{N}}$.

Figure 13 shows the trajectory, aerodynamic and Euler angles. Here again, the different phases of the whole landing are clearly visible in all plots through the detection of the abrupt chagnes in the variable trends. Between seconds 0 and 9, the airplane is descending in trimmed asymmetric conditions, as witnessed by the sideslip and roll angles. At 9 s, the pilot starts the flare and interestingly, as the as pitch angle θ increases, the airplane also experiences a decrease in the roll angle ϕ. This is due to the fact that the pull-up performed with non-null sideslip angle also affects the lateral degrees of freedom. Finally, as the airplane is breaking, the sideslip angle increases dramatically due to the fact that the crosswind component becomes greater than the longitudinal airplane speed. The touchdown occurs at second 20, leading to visible oscillations in α, θ and γ. Subsequently, between seconds 20 and 34, the behavior of the airplane during the ground roll is visible until the complete airplane stop.

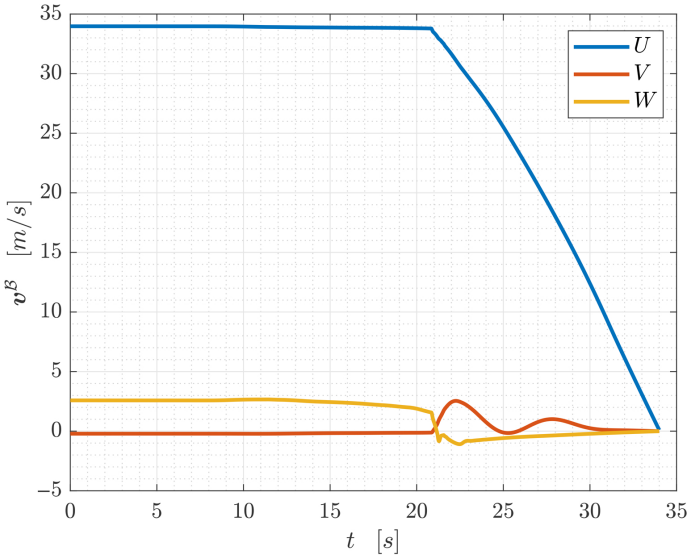

Figure 12. Aircraft velocity components in the body reference frame.

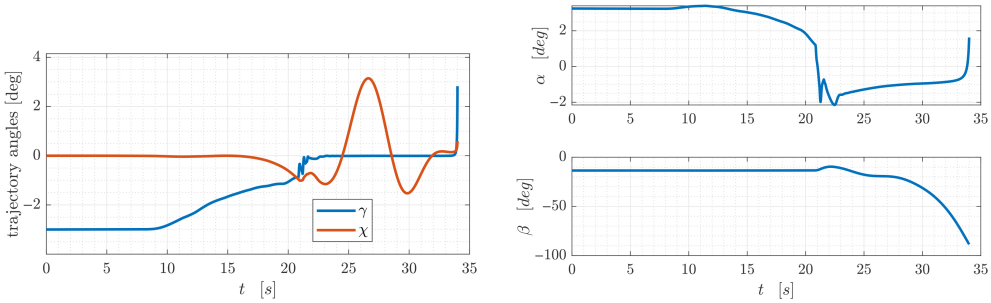

(**a**) Trajectory angles (**b**) Aerodynamic angles

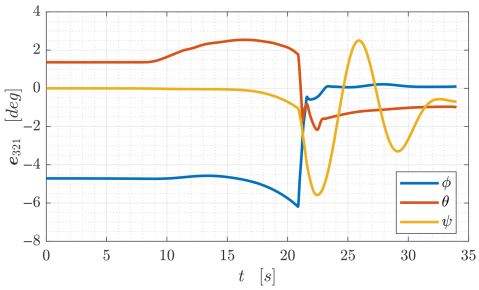

(**c**) Euler angles

Figure 13. Trajectory, aerodynamic and Euler angles in the sideslip landing.

To better show the asymmetry in the landing, Figure 14 displays the deflections of the landing gears and tires. Clearly, the left gear impacts the terrain first, at second 21, while right and nose gears touch the runway about 0.5 s later. Additionally, Figure 15 shows the lateral forces acting on each landing gear F_y (top plots) and the lateral wheel velocities V_y (bottom plots). The left and right landing gears are displayed in the left and center plots, while the nose gear is displayed in the right plot. From the time histories, one may observe the different forces exerted on each leg and the oscillations, which are more visible in the left gear that touches the ground first.

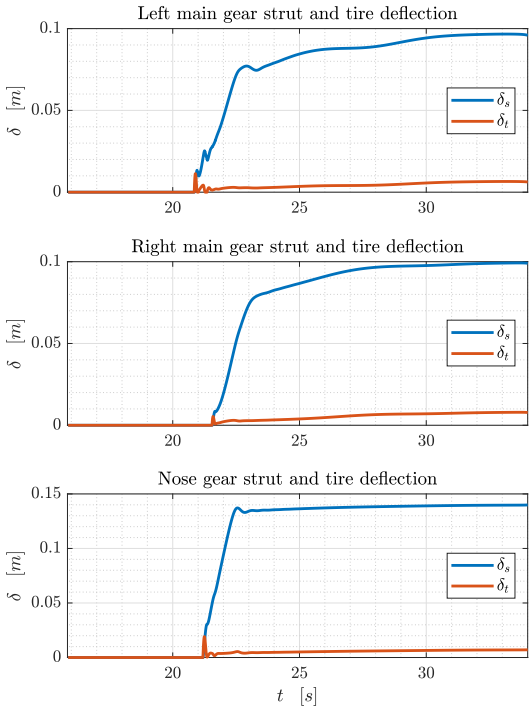

Figure 14. Landing gear deformations in the sideslip landing.

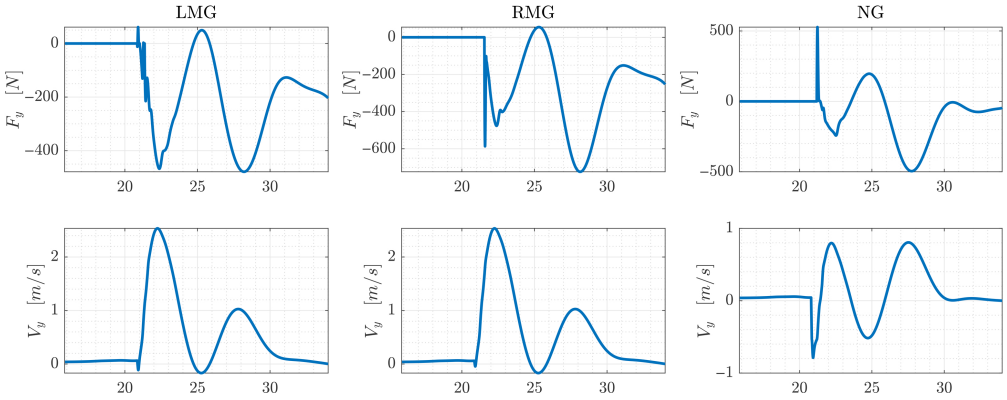

(**a**) Left main gear (**b**) Right main gear (**c**) Nose gear

Figure 15. Landing gear lateral force and velocity in the sideslip landing.

6. Parametric Study of Sideslip Landing Maneuver in Crosswind Conditions

The results described in Sections 5.1 and 5.2 suggest that the simulator linked to the aerodynamic database (Section 3) can be used profitably to perform realistic simulations of entire terminal maneuvers, considering the control inputs provided by a pilot and including the airplane rest state on ground.

At this point, we can perform a parametric study to analyze the landing maneuvers in terms of crosswind and approach speeds. The analysis considers several key performance indicators associated with flight mechanics quantities, loading and safety. In particular, the maximum lateral force exchanged between the ground and the landing gear, the minimum wingtip clearance, the maximum deviation from the runway centerline, the maximum nose wheel steering angle and the landing distance are analyzed. The minimum tip clearance is computed taking into account the actual orientation of the aircraft, with its roll, pitch and heading angles, and the deformation of each landing gear and tire, as depicted in Figure 16, showing a snapshot of the airplane during a landing with 10 deg of roll angle.

Both analyses are performed considering the sideslip landing case, i.e., when the airplane approach is made with the heading aligned with the runway direction, as in Section 5.3.

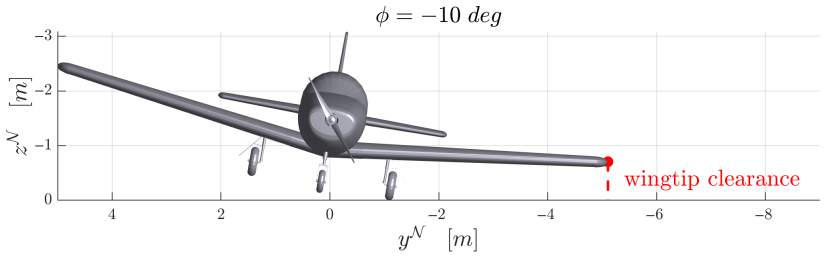

Figure 16. The wingtip clearance is positive for a touchdown with $\phi = -10$ deg.

Table 7 reports the initial variables for all landing simulations of the parametric analysis.

Table 7. Conditions for the simulations of the landing parametric analysis.

Parameter	Symbol	Value
Initial airplane height	h_0	20 m
Track angle and runway direction	χ, χ_{runway}	0 deg
Descent angle	γ_d	3 deg
Flaps deflection	δ_F	40 deg
Landing gear position	δ_G	full down
Heading angle	ψ_{trim}	0 deg
Flight speed	V_{TAS}	30–44 m/s
Northward wind component	v_{WN}	0 m/s
Eastward wind component	v_{WE}	0–14 m/s
Vertical wind component	v_{WD}	0 m/s

Figure 17 reports the most significant key indicators as functions of both the lateral wind component and approach speed. It should be noted that some combinations of low airspeeds and high crosswind speeds are not associated with the performance indices, because in such conditions it was not possible to find an equilibrium point due to limitations or stalling of lateral-directional surfaces and controls. A close look at the results allows us to derive some relevant considerations.

The minimum wingtip clearance remains positive for each combination of airspeed and crosswind speed, with crosswind being the variable that most affects the index. Notice that the clearance is also satisfied with a lateral wind equal to 14 m/s, corresponding to nearly 150% of the maximum demonstrated value. Clearly, for that lateral wind value, the approach speed should be increased up to 40 m/s to ensure lateral-directional equilibrium in the approach phase.

The maximum lateral force exerted on the landing gear becomes higher as the lateral wind grows. A notable result, however, is that, for a given lateral wind value, increasing the landing speed is beneficial to minimize the lateral forces exerted on landing gears. This effect is certainly due to the reduction in the sideslip angle entailed by the increment in the approach speed.

From the results, it is possible to assess that both the maximum lateral deviation and the maximum steering angle do not represent issues, as their values are limited.

The landing distance clearly shows a strong dependence on the landing speed and the wind speed. In particular, increasing the lateral wind and approach speed entails an increase in the landing distance as opposed to what happens for the wingtip clearance and lateral landing gear force. Therefore, wingtip clearance, landing gear loads and landing

distance represent three competing goals in optimizing the landing maneuvers. Clearly, if the runway is long enough, it is advisable to land at higher speeds.

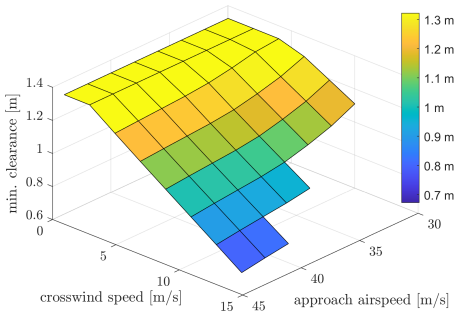

(**a**) Minimum wingtip clearance

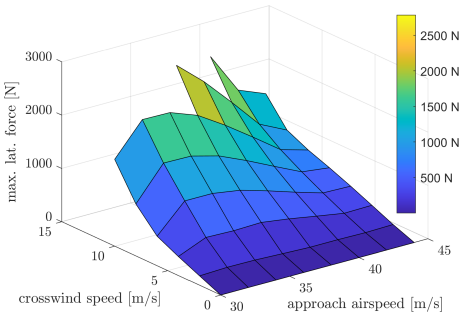

(**b**) Maximum landing gear lateral force

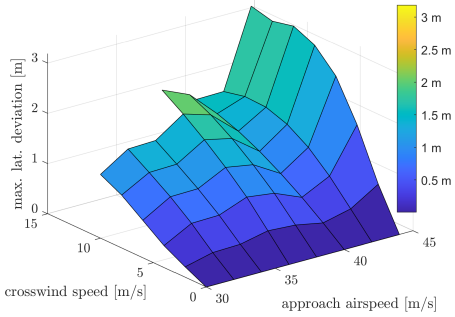

(**c**) Maximum deviation from the runway centerline

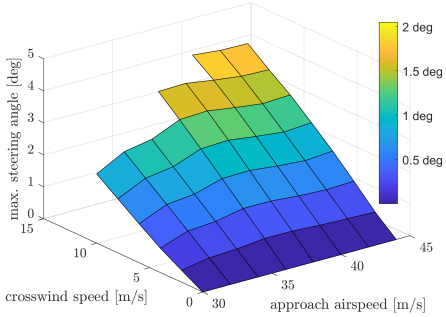

(**d**) Maximum nose wheel steering angle

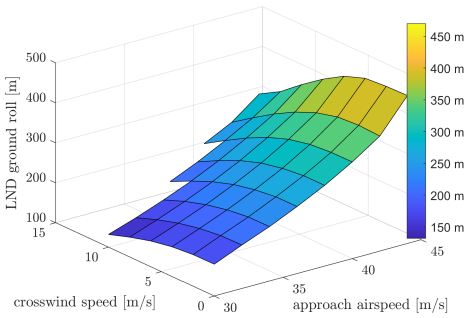

(**e**) Landing distance

Figure 17. Maximum wingtip clearance, maximum landing gear lateral force, maximum deviation with respect to the runway centerline, maximum nosewheel steering angle and landing distance, as functions of the approach speed and the lateral wind speed.

7. Conclusions and Outlook

A flight dynamics simulator has been developed, coupled with landing gear dynamics and with a simple control emulating the presence of a pilot, capable of simulating any flight phase, including terminal maneuvers. The nonlinear aerodynamic characteristics of the airplane are obtained through a dedicated set of Datcom analyses that generate a database accounting for ground effect. The use of nonlinear aerodynamics, unlike linearized models, avoids introducing additional errors caused by deviations from the equilibrium point around which the linear model is built. The presence of the pilot acting on all control surfaces, throttle and nose wheel steering is replicated by a simple controller, which allows

for the simulation of an entire flight, from rest condition before takeoff to rest condition after landing. The tool also accounts for wind, without introducing significant simplifications into the dynamics and aerodynamics modeling.

A parametric study further demonstrated that, with the aerodynamic and landing gear models used in the simulations, the reference Navion airplane can perform landings in crosswind conditions exceeding the demonstrated maximum limits for the aircraft, without veering off the runway, tipping over, or striking the wingtip. These studies also showed that, to reduce lateral forces on the landing gear, typical of asymmetric landings in crosswind conditions, it is advisable to land at higher speeds. In fact, for a given crosswind speed, the maximum value of the lateral gear force reaches a maximum at an approach speed slightly higher than 30 m/s, but consistently reduces as the approach speed increases. This happens because, for a given crosswind speed, higher approach speeds are associated with a lower sideslip angle, with a beneficial impact on most of the landing indicators. However, higher approach speeds also entail longer landing distances, which must be carefully evaluated in terms of the available runway length.

In terms of possible extensions of the proposed work, one should certainly consider the simulations of the terminal maneuvers of airplanes of varying dimensions and weights, in order to assess whether the results of the present analysis remain valid for other aircraft types. Furthermore, a broader validation of the database, generated with the procedure described in this work, should be carried out. Given the complexity of the database, which includes ground effect and sideslip, such validation represents an essential yet non-trivial task.

The simulator and aerodynamic estimation tool could be used for synthesizing and evaluating the performance of a comprehensive automatic control system for rejection of gusts. Additionally, the aerodynamic estimation tool can be employed to assist preliminary aircraft optimization designs.

Author Contributions: Conceptualization, S.C.; Methodology, S.C. and A.C.; Software, A.C.; Validation, A.C.; Formal analysis, S.C. and A.C.; Investigation, S.C.; Data curation, A.C.; Writing—original draft, S.C. and A.C.; Writing—review & editing, S.C. and A.C.; Visualization, A.C.; Supervision, S.C. All authors have read and agreed to the published version of the manuscript.

Funding: This research received no external funding.

Institutional Review Board Statement: Not applicable.

Informed Consent Statement: Not applicable.

Data Availability Statement: The aerodynamic database of the reference airplane generated through Datcom is available for download at https://doi.org/10.5281/zenodo.18508079 [28].

Conflicts of Interest: The authors declare no conflicts of interest.

References

1. Airbus. *A Statistical Analysis of Commercial Aviation Accidents, 1958–2021*; Technical Report; Airbus: Blagnac, France, 2021.
2. Boeing Commercial Airplanes. *Statistical Summary of Commercial Jet Airplane Accidents: World Wide Operations 1959–2015*; Technical Report; Boeing Commercial Airplanes, Aviation Safety: Seattle, WA, USA, 2015.
3. Flight Safety Foundation. *Approach-and-Landing Accident Reduction (ALAR) Briefing Note: 8.7—Crosswind Landing*; Flight Safety Foundation: Alexandria, VA, USA, 2000.
4. Cui, E.; Zhang, X. Ground Effect Aerodynamics. In *Encyclopedia of Aerospace Engineering*; John Wiley & Sons, Ltd.: Hoboken, NJ, USA, 2010. [CrossRef]

5. Dreier, M.E. *Introduction to Helicopter and Tiltrotor Simulation*; AIAA (American Institute of Aeronautics and Astronautics): Reston, VA, USA, 2007.
6. Evans, P.E. Modeling and Simulation of Tricycle Landing Gear at Normal and Abnormal Conditions. Master's Thesis, West Virginia University, Morgantown, WV, USA, 2010. Available online: https://researchrepository.wvu.edu/etd/2153/ (accessed on 23 December 2025).
7. Wang, C.; Holzapfel, F. Modeling of the Aircraft Landing Behavior for Runway Excursion and Abnormal Runway Contact Analysis. In Proceedings of the 2018 AIAA Modeling and Simulation Technologies Conference, Kissimmee, FL, USA, 8–12 January 2018.
8. Daniels, J.N. *A Method for Landing Gear Modeling and Simulation with Experimental Validation*; Technical Report; NASA Contractor Report 201601; NASA Langley Research Center: Hampton, VA, USA, 1996.
9. Yang, X.; Yang, J.; Zhang, Z.; Ma, J.; Sun, Y.; Liu, H. A Review of Civil Aircraft Arresting System for Runway Overruns. *Prog. Aerosp. Sci.* **2018**, *102*, 99–121. [CrossRef]
10. Barnes, A.; Yager, T. *Enhancement of Ground Handling Simulation Capability*; Advisory Group for Aerospace Research and Developement: Neuilly-sur-Seine, France, 1998.
11. Vechtel, D. How Future Aircraft Can Benefit from a Steerable Main Landing Gear for Crosswind Operations. *CEAS Aeronaut. J.* **2019**, *11*, 417–429. Available online: https://link.springer.com/article/10.1007/s13272-019-00410-4 (accessed on 1 February 2026). [CrossRef]
12. Vechtel, D.; Meissner, U.; Hahn, K. On the Use of a Steerable Main Landing Gear for Crosswind Landing Assistance. *CEAS Aeronaut. J.* **2014**, *5*, 293–303. Available online: https://link.springer.com/article/10.1007/s13272-014-0107-2 (accessed on 1 February 2026). [CrossRef]
13. Lei, Z.; Jiang, H.; Li, H. Object-oriented landing gear model in a PC-based flight simulator. *Simul. Model. Pract. Theory* **2008**, *16*, 1514–1532. [CrossRef]
14. Wen, Z.; Zhi, Z.; Qidan, Z.; Shiyue, X. Dynamics Model of Carrier-based Aircraft Landing Gears Landed on Dynamic Deck. *Chin. J. Aeronaut.* **2009**, *22*, 371–379. [CrossRef]
15. Cacciola, S.; Riboldi, C.E.D.; Generali, E. Optimization of Airplane Landing in Crosswind Conditions for Minimum Tire Wear. *Machines* **2023**, *11*, 599. [CrossRef]
16. Fink, R. *USAF Stability and Control DATCOM*; Technical Report AFWAL-TR-83-3048; McDonnell Douglas Astronautics Company: St. Louis, MO, USA, 1978.
17. Cacciola, S.; Testa, L.; Saponi, M. A Procedure for Developing a Flight Mechanics Model of a Three-Surface Drone Using Semi-Empirical Methods. *Aerospace* **2025**, *12*, 515. [CrossRef]
18. Suit, W.T. *Aerodynamic Parameters of the Navion Airplane Extracted from Flight Data*; NASA Technica Note; NASA Langley Research Center: Hampton, VA, USA, 1972.
19. Company, R.A. *Navion Service Manual*; Technical Report; Ryan Aeronautical Company: San Diego, CA, USA, 1949.
20. Roskam, J. *Airplane Design*; Number pt. I–VIII in Airplane Design; DARcorporation: Lawrence, KS, USA, 1997.
21. Raymer, D.P. *Aircraft Design: A Conceptual Approach*; American Institute of Aeronautics and Astronautics: Reston, VA, USA, 2018.
22. Williams, J.E.; Vukelich, S.R. *The USAF Stability and Control Datcom Users Manual*; McDonnell Douglas Astronautics Company: St. Louis, MO, USA, 1979; Volume 1; Updated in 1999.
23. Sereez, M.; Abramov, N.; Goman, M.G. Impact of ground effect on airplane lateral directional stability during take-off and landing. *Open J. Fluid Dyn.* **2018**, *8*, 1–14. [CrossRef]
24. O'Leary, C.O. *Flight Measurements of Ground Effect on the Lift and Pitching Moment of a Large Transport Aircraft (Comet 3B) and Comparison with Wind Tunnel and Other Data*; Aerodynamics Department, R.A.E. Bedford: Bedford, UK, 1969.
25. Chaney, V.; Vaux, S.; Bolds-Moorehead, P.; Lutz, T. Joint Airbus and Boeing Flight Test Lecture. Royal Aeronautical Society, Flight Test Group, 2013. Historic Joint Lecture by Airbus and Boeing Test Pilots and Flight Test Engineers. Royal Aeronautical Society Headquarters, London, 14 March 2013. Available online: https://www.youtube.com/watch?v=HVt6LiDbLos (accessed on 1 February 2026).
26. AOPA. Seeing Is Believing. Yes, This Is a 1947 Navion. Available online: https://www.aopa.org/news-and-media/all-news/2016/june/pilot/1947-navion (accessed on 1 February 2026).
27. Roskam, J. *Airplane Design. Pt 6*; Design Analysis and Research Corporation: Lawrence, KS, USA, 1987.
28. Cacciola, S.; Calabria, A. Figures and data: Nonlinear Simulation of Terminal Maneuvers including Landing Gear Dynamics, Crosswind and Ground Effect. In *Applied Sciences*; Zenodo: Genève, Switzerland, 2026. Available online: https://zenodo.org/records/18508079 (accessed on 1 February 2026).

29. MATLAB. *MATLAB R2024b Release Docmentation*; The MathWorks Inc.: Natick, MA, USA, 2024.
30. Biannic, J.M.; Roos, C. *Robust Autoland Design by Multi-Model $\mathcal{H}_\infty$ Synthesis with a Focus on the Flare Phase*; Systems & Information Processing Department, The French Aerospace Lab (ONERA): Palaiseau, Franve, 2018.